Inorganic Chemistry
Article
Cite This: Inorg. Chem. XXXX, XXX, XXX−XXX
pubs.acs.org/IC

High-Valent d^7 Ni^{III} versus d^8 Cu^{III} Oxidants in PCET

Duenpen Unjaroen,[†] Robert Gericke,[†,§] Marta Lovisari,[†,§] Daniel Nelis,[†,§] Prasenjit Mondal,[†] Paolo Pirovano,[†] Brendan Twamley,[†] Erik R. Farquhar,[‡] and Aidan R. McDonald[*,†]

[†]School of Chemistry, Trinity College Dublin, The University of Dublin, College Green, Dublin 2, Ireland
[‡]Case Western Reserve University Center for Synchrotron Biosciences, National Synchrotron Light Source II, Brookhaven National Laboratory II, Upton, New York 11973, United States

Supporting Information

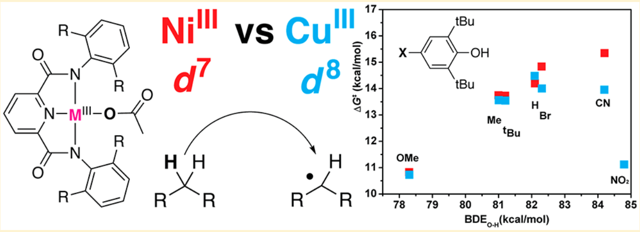

ABSTRACT: Oxygenases have been postulated to utilize d^4 Fe^{IV} and d^8 Cu^{III} oxidants in proton-coupled electron transfer (PCET) hydrocarbon oxidation. In order to explore the influence the metal ion and d-electron count can hold over the PCET reactivity, two metastable high-valent metal−oxygen adducts, [Ni^{III}(OAc)(L)] (**1b**) and [Cu^{III}(OAc)(L)] (**2b**), L = *N*,*N*′-(2,6-diisopropylphenyl)-2,6-pyridinedicarboxamidate, were prepared from their low-valent precursors [Ni^{II}(OAc)(L)]$^-$ (**1a**) and [Cu^{II}(OAc)(L)]$^-$ (**2a**). The complexes **1a**/**b**−**2a**/**b** were characterized using nuclear magnetic resonance, Fourier transform infrared, electron paramagnetic resonance, X-ray diffraction, and absorption spectroscopies and mass spectrometry. Both complexes were capable of activating substrates through a concerted PCET mechanism (hydrogen atom transfer, HAT, or concerted proton and electron transfer, CPET). The reactivity of **1b** and **2b** toward a series of *para*-substituted 2,6-di-*tert*-butylphenols (*p*-X-2,6-DTBP; X = OCH$_3$, C(CH$_3$)$_3$, CH$_3$, H, Br, CN, NO$_2$) was studied, showing similar rates of reaction for both complexes. In the oxidation of xanthene, the d^8 Cu^{III} oxidant displayed a small increase in the rate constant compared to that of the d^7 Ni^{III} oxidant. The d^8 Cu^{III} oxidant was capable of oxidizing a large family of hydrocarbon substrates with bond dissociation enthalpy (BDE$_{C-H}$) values up to 90 kcal/mol. It was previously observed that exchanging the ancillary anionic donor ligand in such complexes resulted in a 20-fold enhancement in the rate constant, an observation that is further enforced by comparison of **1b** and **2b** to the literature precedents. In contrast, we observed only minor differences in the rate constants upon comparing **1b** to **2b**. It was thus concluded that in this case the metal ion has a minor impact, while the ancillary donor ligand yields more kinetic control over HAT/CPET oxidation.

INTRODUCTION

Oxidative activation of inert hydrocarbon C−H bonds represents a very powerful transformation with the potential for large-scale production of functionalized hydrocarbons.[1,2] The ability to readily convert natural gas and petroleum derived hydrocarbons into higher-value oxidized products (alcohols, aldehydes, olefins) is both environmentally and economically much sought after. To this end, catalysts based on cheap and abundant first-row transition metals capable of oxidative activation of saturated hydrocarbons under ambient conditions are highly desirable.

Mn-, Fe-, Ni-, and Cu-containing metalloenzymes perform oxidative activation of hydrocarbons, yielding oxygenated and desaturated products.[3−8] For many of these metalloenzymes, activation of the saturated C−H bond occurs through hydrogen atom transfer (HAT) by a high-valent oxidant, normally a metal−oxygen adduct.[3,9−14] The hydrogen atom is transferred from the substrate to a high-valent metal−oxo, −hydroxide, or −bis-*μ*-oxo adduct, yielding the respective hydroxide, aquo, or hydroxide products, a reaction that falls under the category of proton-coupled electron transfer (PCET).

There still exists minimal insight into the influence of the specific metal ion in such HAT reactions, that is, how isostructural Mn vs Fe vs Ni vs Cu oxidants should fare in performing HAT oxidation of the same substrates. For example, nonheme iron oxygenases are postulated to employ a mono- or dinuclear d^4 Fe^{IV} oxidant to facilitate hydrocarbon oxidation, while copper hydroxylases are often postulated to oxidize via a mono- or dinuclear d^8 Cu^{III} oxidant.[3−8] Both Fe- and Cu- containing metalloenzymes and zeolite supported Fe and Cu catalysts have been demonstrated to be capable of activating the strong C−H bond of methane (C−H bond dissociation enthalpy (BDE$_{C-H}$) = 104.9 kcal/mol).[3−8,15,16] This suggests that both harder, low d-electron count, and softer, high d-electron count, transition metal oxidants are capable of driving the oxidation of the most thermodynamically challenging of substrates. This was addressed in part by Mayer who performed a direct comparison of Fe, Co, and Ru oxidants in HAT reactions, showing that the ground-state entropic effects influenced HAT.[15−18] We have posed the

Received: October 22, 2019

DOI: 10.1021/acs.inorgchem.9b03101
Inorg. Chem. XXXX, XXX, XXX−XXX

question, should there be situations where one would choose one metal over another?

The magnitude of the O−H bond dissociation free energy ($BDFE_{O-H}$) in the respective hydroxide, aquo, or hydroxide products governs the thermodynamic driving force for C−H activation. The redox potential of the high-valent oxidant and the pK_a of the O−H entity in the product (Scheme 1) determine the magnitude of the $BDFE_{O-H}$.[19−21] We postulate that harder, early transition metal entities are likely to display relatively high redox potentials and relatively low pK_a values due to their relatively low electron affinity and electronegativity. Softer late transition metal entities may display relatively high pK_a values and low redox potentials, due to their high electron affinity and electronegativity. This led us to consider the effect different transition metal ions may hold over $BDFE_{O-H}$ and the possibility of a direct like-for-like comparison of isostructural high-valent oxidants with different metal ions in oxidation reactions.

Scheme 1. HAT and CPET by High-Valent Metal-Carboxylate Complexes

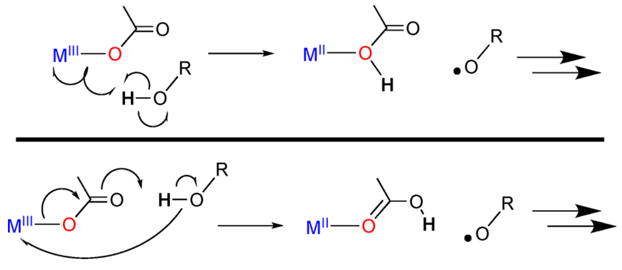

We recently reported the preparation and characterization of a family of terminal Ni^{III}−oxygen adducts (Scheme 2), $[Ni^{III}(OX)(L^*)]$ (OX = OCO_2H, O_2CCH_3 (OAc), and ONO_2), supported by *N*,*N*′-(2,6-dimethylphenyl)-2,6-pyridinedicarboxamidate (L*).[22−25] We observed a 20-fold enhancement in the rate constant for HAT oxidation upon exchanging ONO_2 for OAc. Having gained an understanding of the anionic ancillary ligand (OX in $[Ni^{III}(OX)(L^*)]$) in HAT oxidations, and herein we explore the role of the metal ion, d^7 Ni^{III} versus d^8 Cu^{III}, in driving PCET oxidation of a variety of substrates.

Scheme 2. Generation of d^7 Ni^{III} 1b and d^8 Cu^{III} 2b by Oxidation of 1a/2a with Tris(4-bromophenyl) Ammoniumyl Hexachloroantimonate (Magic Blue)

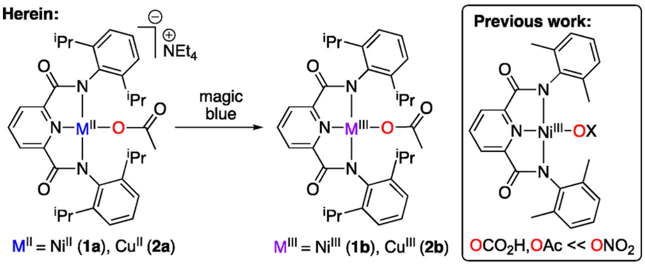

■ RESULTS AND DISCUSSION

Synthesis and Characterization of 1a and 2a. $[Ni^{II}(OAc)(L)]Et_4N$ (**1a**, OAc = O_2CCH_3; L = *N*,*N*′-(2,6-diisopropylphenyl)-2,6-pyridinedicarboxamidate, Scheme 2) was prepared via a two-step synthesis comparable to a previously reported procedure for the synthesis of $[Ni^{II}(OAc)(L^*)]Et_4N$ (L* = *N*,*N*′-(2,6-dimethylphenyl)-2,6-pyridinedicarboxamidate, see Supporting Information for details).[23] $NiCl_2$ was reacted with LH_2 in the presence of $NaOCH_3$ and CH_3CN to form the $[Ni^{II}(NCCH_3)(L)]$ complex (**3**, 70% yield).[26] The CH_3CN ligand was then replaced by the addition of tetraethylammonium acetate (Et_4NOAc, 1.1 equiv) to yield **1a** in 73% yield. **2a** was prepared from the previously reported $[Cu^{II}(NCCH_3)(L)]$[27] in a similar fashion (60% yield). ^1H and ^{13}C nuclear magnetic resonance (NMR) spectroscopy, electrospray ionization mass spectrometry (ESI-MS), Fourier transform infrared (FT-IR), and electron paramagnetic resonance (EPR) spectroscopies and X-ray crystallography data supported the formation of complexes **1a** and **2a** (Figure 1, Figures S1−S5).

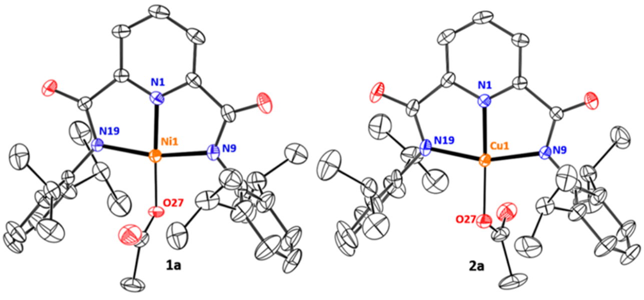

Figure 1. ORTEPs (at 50% probability level) of the X-ray crystallographically determined structures of **1a** and **2a**. Hydrogen atoms and counterions have been omitted for clarity.

Crystals of **1a** and **2a** suitable for X-ray diffraction measurements were obtained by layering CH_3CN solutions of the complexes with diethyl ether (Et_2O). The crystal structures of both molecules showed the central metal ion coordinated in a square planar environment with three N donors from the 2,6-pyridinedicarboxamidate ligand and a monodentate O atom donor from the OAc anion (Tables S1 and S2). The τ_4 parameters for **1a** and **2a** were 0.18 and 0.26, respectively, which indicated that the complexes were in slightly distorted square planar geometries (τ_4 = 0 for pure square planar, τ_4 = 1 for pure tetrahedral).[28] The geometric parameters of **1a** and **2a** were similar to those of previously reported $[Ni^{II}(OX)(L^*)]^-$ (OX = OH, OCO_2H, OAc, ONO_2) and $[Cu^{II}(OH)(L)]^-$ complexes.[22,23,25,27,29]

Preparation and Characterization of 1b and 2b. $[Ni^{III}(OAc)(L)]$ and $[Cu^{III}(OAc)(L)]$ (**1b** and **2b**) were generated using the one-electron oxidant magic blue (tris(4-bromophenyl)ammoniumyl hexachloroantimonate) as an oxidant. Solutions of **1a** (0.3 mM) and **2a** (0.25 mM) in acetone were cooled to −40 °C, followed by the addition of magic blue (exactly 1 equiv, as a 7.5 mM CH_3CN solution) resulting in an immediate reaction (complete within 2 s for both complexes, Figure 2). Titration of magic blue demonstrated a maximum yield of **1b**/**2b** with 1 equiv of oxidant (Figure 2). ESI-MS showed the expected elemental formula for the high-valent species (Figure S6). At −40 °C the complexes showed no substantial decay over the course of an hour (**1b**, $t_{1/2}$= 4 h; **2b**, $t_{1/2}$= 22 h). Complex **2b** could also be generated in high yield at 25 °C, using magic blue, demonstrating a $t_{1/2}$ = 70 min at 25 °C. Compound **1b** was thermally unstable upon preparation at 25 °C with magic blue,

DOI: 10.1021/acs.inorgchem.9b03101

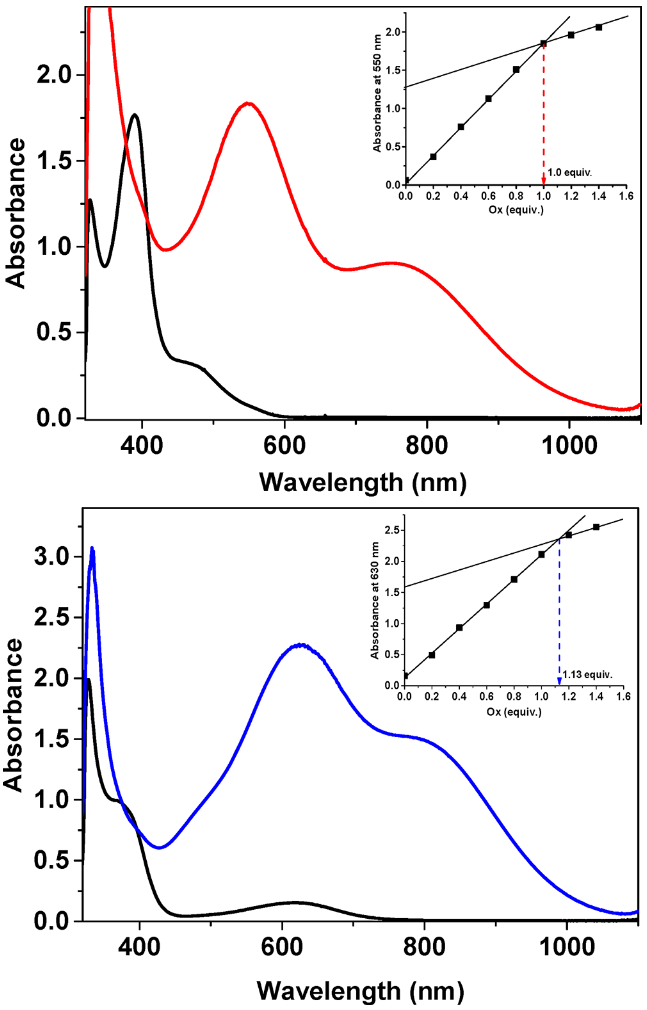

Figure 2. Electronic absorption spectra in acetone at −40 °C. (Top) **1a** (black trace, 0.3 mM) and **1b** (red trace); (bottom) **2a** (black trace, 0.25 mM) and **2b** (blue trace). The insets show the titration of magic blue with **1a** (top) and **2a** (bottom) monitored by plotting the intensity of the λ = 550 nm for **1a** and λ = 630 nm for **2a** versus equivalents of magic blue. The continued increase in absorbance beyond 1 equiv is attributed to the magic blue oxidant.

it was obtained in 50% yield and decayed within 120 s after the addition of magic blue. Furthermore, when NaOCl/AcOH was employed as an oxidant, **1b** was unstable (decay within 20 s at 25 °C, Figure S7). This contrasts with the previously reported [Ni^{III}(OAc)(L*)] complex which was thermally stable at 25 °C when prepared with NaOCl/AcOH.[23] The instability may be attributed to ligand oxidation (at the isopropyl group) which we previously observed for L,[26] but not for L*.[22,23,25]

The electronic absorption spectrum of **1b** showed two intense features at λ_{max} = 550, 760 nm (Figure 2) which were very similar to the features observed for the previously reported [Ni^{III}(OAc)(L*)] (λ_{max} = 510 nm, 760 nm, Figure S8).[23] The red shift in the higher-energy band of **1b** is presumably a result of the different substituents on the aryl amidate donors (L = 2,6-diisopropylphenyl; L* = 2,6-dimethylphenyl). Such features are a hallmark of Ni^{III} complexes supported by 2,6-pyridinedicarboxamidate donors[23] and are also generally typical of Ni^{III} complexes.[22−26,30−33] Compound **2b** also displayed two intense bands in the visible and NIR regions of its electronic absorption spectrum at λ_{max} = 630, 805 nm (Figure 2). Tolman's [Cu^{III}(OH)(LX)] complexes displayed a single intense visible band at λ_{max} = 540 nm,[34−38] whereas **2b** showed two absorption bands at lower energies, presumably as a result of the weaker-field donor ancillary ligand (OAc for **2b**, versus OH in [Cu^{III}(OH)(LX)]). On the basis of the electronic absorption properties of **1b** and **2b**, we assign them the respective structures [Ni^{III}(OAc)(L)] and [Cu^{III}(OAc)(L)].

Electron paramagnetic resonance (EPR) spectroscopy analysis of **1b** showed the presence of two sets of signals that can be attributed to two S = 1/2 d^7 Ni^{III} ions (Figure 3, see Supporting Information for details). One set displayed an axial signal ($g_{\perp}$ = 2.24, $g_{\parallel}$ = 2.02, g_{av} = 2.17) and the other a more rhombic signal (g_x = 2.40, g_y = 2.28, g_z = 2.00, g_{av} = 2.23). The relative ratio of the signals were 70% for the axial component and 30% for the rhombic component. The overall yield of Ni^{III} in the reaction mixture was 80 ± 20% (with respect to [**1a**]), determined by the comparison of the double integral of the entire signal to that of a TEMPO ((2,2,6,6-tetramethylpiperidin-1-yl)oxyl) standard. The axial component was remarkably similar to those identified for previously reported [Ni^{III}(OX)(L*)] complexes (OX = OCO_2H, OAc, ONO_2).[23] This led us to assign the axial signal to that of [Ni^{III}(OAc)(L)]. The rhombic component as of yet cannot be identified. The previously prepared [Ni^{III}($O_2CC_6H_4Cl$)(L)] displayed a remarkably similar rhombic EPR signal.[26] The different signals may represent different binding modes of the OAc ligand, monodentate versus bidentate.

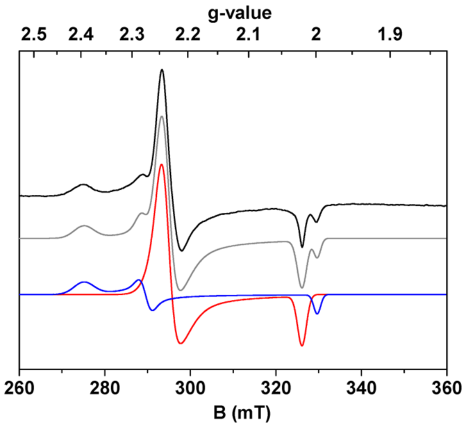

Figure 3. EPR spectra of frozen solutions of **1b** (black line), obtained by the oxidation of **1a** with NaOCl/AcOH (15 equiv) or magic blue (1 equiv), and simulated EPR spectra of **1b** (gray line). The simulation is made up of two S = 1/2 signals: blue trace, rhombic component; red trace, axial component. The spectrum was acquired from a frozen acetone solution, measured at 77 K, 2.02 mW microwave power, with 0.3 mT modulation amplitude.

The EPR spectrum of **2a** displayed a signal typical of [Cu^{II}(L)] complexes (Figure S9).[27,34,36,37] The EPR spectrum of **2b** was found to be almost silent, with a residual presence of ~10% of S = 1/2 Cu^{II} ion, as found by comparison to the doubly integrated spectrum of **2a**. This observation is consistent with the conversion of a d^9 Cu^{II} complex (**2a**) to a d^8 Cu^{III} complex (**2b**), with Cu in a square planar environment.

Compound **1b** is a member of a now large family of [Ni^{III}(X)(L*)] complexes that have been explored using X-ray absorption spectroscopy (XAS) analysis.[22−24] Given that the other spectral properties associated with **1b** were remarkably similar to those previously reported, we did not believe XAS analysis of **1b** was warranted. Cu K-edge X-ray absorption near edge structure (XANES) analysis was carried out on **2a** and **2b** to explore the structural and electronic properties of the metastable $\mathrm{Cu^{III}}$ complex. Compound **2a** displayed a 1s → 3d pre-edge transition centered at 8978.1 eV (Figure 4), while **2b** had an equivalent peak at 8979.4 eV, approximately 1.3 eV higher in energy (Figure S10).[39−44] These pre-edge transition energies fall within the expected range for $\mathrm{Cu^{II}}$ and $\mathrm{Cu^{III}}$ complexes, respectively. DuBois et al. showed a shift of 1.0−2.0 eV for $\mathrm{Cu^{II}}$ to $\mathrm{Cu^{III}}$ pairs and demonstrated that this was the only reliable predictor of oxidation state for Cu XANES.[41] Our results are fully consistent with this. The pre-edge features have the same normalized intensity for both **2a** and **2b**, suggesting that there has not been a change in geometry or coordination number. Altering the geometry and so the degree of 3d and 4p mixing would change the intensity of this feature.[45,46] The 1.3 eV blue shift suggested an integer change in the oxidation state of the metal (thus $\mathrm{Cu^{II}}$ to $\mathrm{Cu^{III}}$).[39−44]

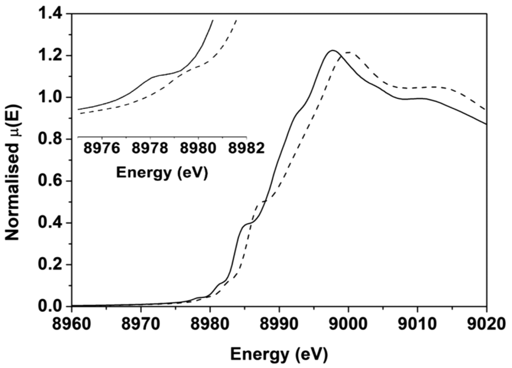

Figure 4. Normalized Cu K-edge spectrum of **2a** (solid trace) and **2b** (dashed trace). Inset: expanded pre-edge region.

Along the rising edge, there were 1s → 4p plus ligand-to-metal-charge-transfer (LMCT) "shakedown" transitions visible at 8984.3 and 8986.7 eV for **2a** and **2b**, respectively (Figure S11, Table S3).[39,41,46] For **2a**, an additional 1s → 4p "main" transition was found at 8992.3 eV, which was not seen in **2b** (Figure S12). The ratio of the main or shakedown second derivative peaks was 4.4 and ~0 for **2a** and **2b**, respectively. Compound **2b** does not have an observable 1s → 4p main peak; the numerator approaches zero in the fraction, leading to an overall value of ~0. It was previously observed that, for a $\mathrm{Cu^{II}/Cu^{III}}$ pair, the ratio of the intensities of the second derivative peaks for the 1s → 4p main or 1s → 4p plus shakedown transitions was found to be ≥1 for $\mathrm{Cu^{II}}$ complexes and then reversed to be ≤1 for the corresponding $\mathrm{Cu^{III}}$ complexes, as was observed for **2a**/**2b**, supporting the assignment of **2b** as containing a $\mathrm{Cu^{III}}$ ion.[41] The rising edge maximum energy was blue-shifted due to the increase in the oxidation state of **2b** relative to **2a**; however, the profile was unaffected. The shape of the rising edge maximum has been postulated to be a consequence of multiple scattering (MS) effects which are dependent on the local geometry around the scattering atom, thus suggesting a retention of geometry upon oxidation of **2a** to **2b**.[47]

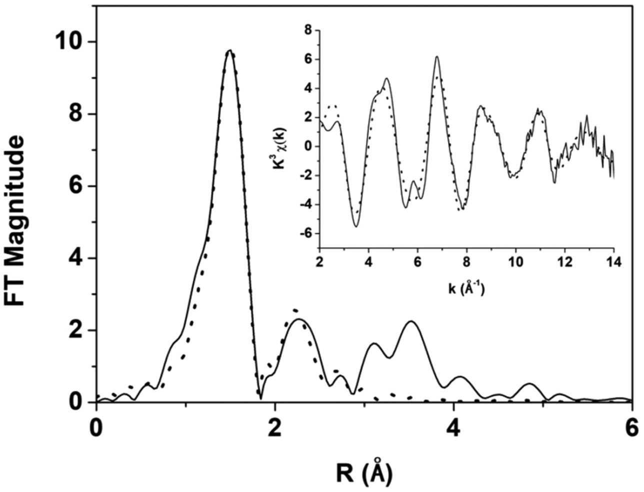

Figure 5. Representative best fit (fit 7 in Table S5) to k^3-weighted EXAFS data of **2b**. Experimental data is shown as a black trace, while the best fit is represented as a dotted trace.

Extended X-ray absorption fine structure (EXAFS, Figure 5) analysis was carried out for both **2a** and **2b**. The best fit for **2a** was found with 4 N/O scatterers at 1.96 Å, suggesting a monodentate coordination of the OAc ion, a 1 C scatterer at 2.51 Å, from the bound OAc, and 4 C scatterers from the carboxamide backbone at 2.85 Å (Table S4, Figure S13). This data matches well with the X-ray crystallography data of the complex (Table S2). Similarly, the best fit of the data for **2b** was obtained with 4 N/O scatterers at 1.88 Å, suggesting a monodentate coordination of the OAc ion, 1 C/O scatterer at 2.38 Å, and 4 C scatterers at 2.76 Å (Table S5). When comparing **2a** to **2b**, the average bond lengths of the first-coordination sphere metal−scatterer distances decreased by 0.08 Å (Tables S4 and S5). This can be attributed to an increase in the oxidation state, and thus positive charge, of the copper atom. From the XANES and EXAFS data, **2b** can be assigned as the one-electron oxidized equivalent of **2a** with retention of the square planar geometry around the absorbing nucleus.

Quantum chemical calculations at the DFT uM06L cc-pVTZ (C, H, N, O)/SDD (Ni, Cu) level of theory were performed to give theoretical support to the XAS-measured structure of **2b** and to predict a structure for **1b** (Figures S55−S59, Tables S8−S12). The DFT optimized structures of the low-valent complexes **1a** and **2a** showed very minor deviations of the Ni−N/O bond distances (1.880 Å) by about 0.02 Å and Cu−N/O distances (1.991 Å) by approximately 0.03 Å when compared to those of the molecular structures obtained from single crystal X-ray diffraction, demonstrating our DFT methods to be effective for predicting the structures of **1b** and **2b**. For **1b**, two possible coordination modes of the OAc ligand were predicted using DFT, whereby the chelating motive (**1b-chelate**) was more stable than the monodentate structure (**1b-mono**) by ~6 kcal/mol. In **1b-chelate** the spin density was mainly at the Ni core (1.07) with predominantly d_{z^2} character and slightly scattered to the apical O atom (0.15), while in **1b-mono** the Mulliken spin density (Figure S60) was mainly at the Ni core (0.67) with predominantly d_{xz} character and scattered over the amide N atoms (0.11). This observation is consistent with previous DFT predicted electronic structures for $[\mathrm{Ni^{III}(OAc)(L^*)}]$.[23] The average Ni−N/O bond lengths in the basal plane are elongated from **1b-mono** (1.87 Å) to **1b-chelate** (1.92) by about 0.05 Å as expected, and the apical Ni···O separation is shortened by about 0.55 Å from the

Table 1. Spectroscopic and Reactivity Properties of **1b**, **2b**, and [Ni^{III}(OAc)(L*)]

	λ_{max} (nm)	$g\perp$, $g_{\parallel}$, g_x, g_y, g_x (g_{av})	M$^{II/III}$$E_{1/2}$ vs Fc$^+$/Fc (V)	M−O (Å)	k_2 for 2,6-DTBP[a]	k_2 for xanthene[a]
1b	550, 760	2.24, 2.02 (2.17)	0.32	1.92[b]	0.24	0.003
[Ni^{III}(OAc)(L*)]	510, 760	2.24, 2.02 (2.17)	0.35	1.92	0.125	0.004
2b	630, 805		0.17	1.88	0.10	0.012

[a] All performed at −40 °C in acetone. [b] Predicted using DFT.

monodentate motive (2.63 Å) toward the chelating motive (2.08 Å).

For **2b**, the OAc ligand was found to bind in a monodentate fashion at Cu. The average Cu−N/O bond lengths were shortened by about 0.08 Å with respect to **2a**, which is in excellent agreement with the EXAFS findings. The Cu···O separation to the apical O atom of the OAc ligand was found to be 2.46 Å, which is too long to be defined as a bond. We have also calculated the highest occupied MO for **1b** and **2b**. On average the HOMO of **2b-mono** was 2.5 kcal/mol lower than that for **1b-chelate**. Overall, DFT calculations support our XAS measurements with regard to metal−ligand bond lengths in **2b** and the coordination geometry and number at Cu^{III} in **2b**.

Reactivity Studies. Complexes **1b** and **2b** were examined for their ability to oxidatively activate phenolic O−H and hydrocarbon C−H bonds. The oxidation reactions were monitored using electronic absorption spectroscopy by following the decay of the absorption bands at λ = 550 nm for **1b** and λ = 630 nm for **2b** against time. In the presence of excess substrate (>10 equiv), pseudo-first-order rate constants (k_{obs}) were obtained by exponential fitting of the decay plots. This allowed for the determination of second-order rate constants (k_2) by plotting k_{obs} against the substrate concentration and calculating the slope of the resultant linear plot.

*Reactivity of **1b** and **2b** with Phenol Substrates.* In order to gain insight into the kinetic and thermodynamic reactivity properties of **1b** and **2b**, the oxidation of *para*-X-2,6-di-*tert*-butylphenol substrates (*p*-X-2,6-DTBP, X = OCH_3, $C(CH_3)_3$, CH_3, H, Br, CN, NO_2) was explored at −40 °C. Upon the addition of 2,6-di-*tert*-butylphenol (2,6-DTBP, 160 equiv in acetone) to **1b** at −40 °C, the bands at λ = 550 and 760 nm decayed within 400 s (Figure S14). The radical coupling product 3,3′,5,5′-tetra-*tert*-butyl-[1,1′-bis(cyclohexylidene)]-2,2′,5,5′-tetraene-4,4′-dione was detected in approximately 10% yield along with 2,6-di-*tert*-butyl-1,4-benzoquinone (Figures S15−S17). A k_2 = 0.24 M^{-1} s^{-1} value was determined (Table 1). Further second-order rate constants ($^{X}k_2$) for the oxidation of various other *p*-X-2,6-DTBP substrates were subsequently determined (Table S6, Figures S18 and S19). For *p*-X-2,6-DTBP, X = OCH_3, $C(CH_3)_3$, H, Br, CN, NO_2 the radical coupling product 3,3′,5,5′-tetra-*tert*-butyl-[1,1′-bis(cyclohexylidene)]-2,2′,5,5′-tetraene-4,4′-dione was detected along with 2,6-di-*tert*-butyl-4-quinone (Figures S21 and S22). For *p*-CH_3-2,6-DTBP the oxidized product was identified as 2,6-di-*tert*-butyl-4-methylene-3,5-cyclohexadien-1-one (Figure S20). The reaction between **1b** and *p*-OCH_3-2,6-DTBP was very rapid, and therefore, k_2 was calculated under stoichiometric conditions (Figure S23, see Supporting Information for details). *p*-NO_2-2,6-DTBP reacted with **1b** displaying a zeroth-order decay, and accurate kinetic analysis was not possible; we therefore excluded it from our analysis. A kinetic isotope effect (KIE) value of 4.4 was obtained from the reactions of **1b** with [*H*]-*p*-CH_3-2,6-DTBP and [*D*]-*p*-CH_3-2,6-DTBP substrates (Figure S24). The measured KIE is consistent with O−H bond cleavage being rate-determining.

To gain further understanding of the mechanism of the reaction between **1b** and *p*-X-2,6-DTBP substrates, we plotted the [$\log(^{X}k_2/^{H}k_2)$] value against the Hammett σ^+-parameter. The Hammett analysis gave a good linear correlation with a negative Hammett ρ value of −2.73 (Figure 6). The slope obtained from this analysis is close to the Hammett correlation slope (ρ = −2.5) for the reaction of [Ni^{III}(Cl)(L*)] with *p*-X-2,6-DTBP substrates where HAT was ascribed.[24] A plot of the $\log(k_2)$ against BDE_{O-H} displayed a linear relationship (Figure S25). A plot of Gibbs energies ($\Delta G^{\ddagger}$) of activation from the k_2 values against BDE_{O-H} displayed a slope of 0.78 (Figure 6, Figure S26). $BDFE_{O-H}$ values for all of these substrates in acetone were not available. For ease of comparison, we have plotted BDE_{O-H} (an enthalpy) against $\Delta G^{\ddagger}$ (a free energy, the differences in BDE and BDFE values are sufficiently small enough that the comparison is valid). The ideal $\Delta G^{\ddagger}/\Delta G^{\circ}$(BDFE) value is 0.5 for HAT.[19−21] The obtained value was comparable, if a little large, with the previously reported examples of metal-based oxidants (0.15 to 0.7) that performed HAT, and close to that for [Ni^{III}(Cl)(L*)] (0.66) where HAT was ascribed for the same family of substrates.[24] In contrast, in an example where nonconcerted PCET was identified, the slope of a comparable plot for the same family of substrates was 0.99.[48] These results indicated that a concerted PCET mechanism was at hand, either HAT or concerted proton and electron transfer (CPET, where the H^+ and e^- travel simultaneously but arrive at different locations).

A Marcus-type plot of $(RT/F)\ln(k_2)$ versus the oxidation potentials (E_{OX}) of the phenols showed a linear correlation which decreased with an increasing of E_{OX}. A slope of −0.18 was obtained (Figure 6). This also indicated a HAT or CPET reaction mechanism.[49−55] If the reaction involved a rate-limiting electron transfer from phenols followed by a fast proton transfer, the slope of the Marcus plot would be expected to be −0.5. If the proton transfer was rate limiting, the slope is predicted be −1.0. A HAT mechanism has been predicted for a slope closer to 0.00. The observed slope thus rules out the nonconcerted PCET mechanisms. Indeed, [Ni^{III}(Cl)(L*)] displayed a slope = −0.15 with the same family of substrates.[24] The combination of the Hammett, Bell−Evans−Polanyi, and Marcus relationships indicated that the reaction of **1b** with phenol substrates occurred via HAT or CPET.

The reactivity of **2b** with phenol substrates was examined under the exact same conditions employed for **1b** (Figures S27−S29). Upon the addition of the phenol substrates to **2b**, the electronic absorption spectrum revealed the decay of the bands at λ = 630, 805 nm, concomitant with an appearance of new bands around λ ~ 400 nm (Figure S27). A comparison of the k_2 values for the oxidation of electron-rich *p*-X-2,6-DTBP (X = OCH_3, CH_3, H) showed almost the same values (**1b**: 343, 0.63, 0.24; **2b**: 403, 1.18, 0.09, respectively, units: M^{-1} s^{-1}) (Figure 6, Table S6). The radical coupling product

DOI: 10.1021/acs.inorgchem.9b03101
Inorg. Chem. XXXX, XXX, XXX−XXX

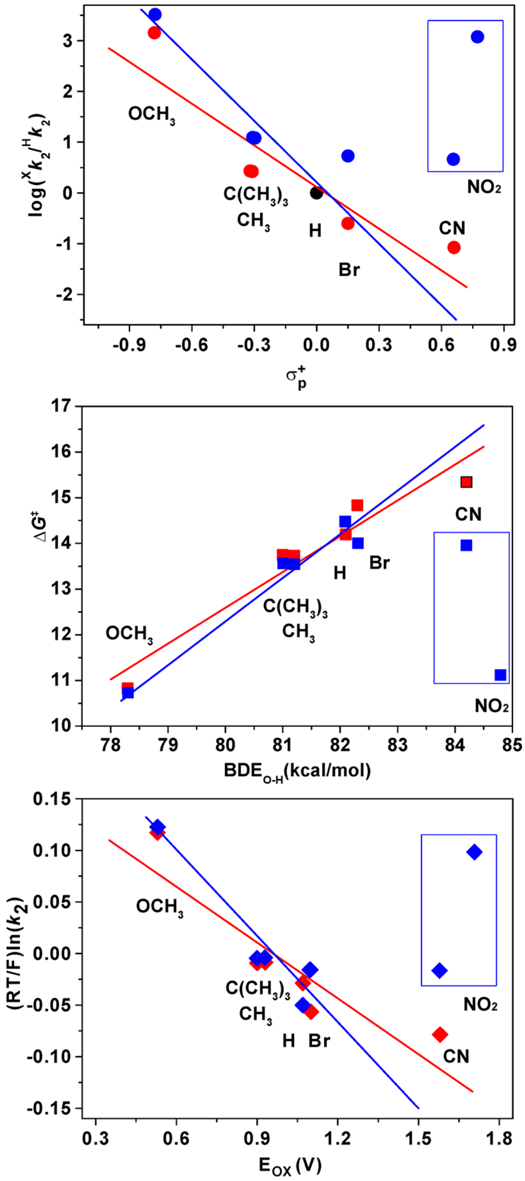

Figure 6. (Top) Hammett correlation plots; (middle) plots of $\Delta G^‡$ against the BDE_{O-H} of the substrates. $\Delta G^‡$ was determined from k_2 via the Eyring equation. Note: $BDFE_{O-H}$ values for all of these substrates in acetone were not available. For ease of comparison, we have plotted BDE_{O-H} (an enthalpy) against $\Delta G^‡$ (a free energy, the differences in BDE/BDFE values are sufficiently small for those available that the comparison is valid). BDE_{O-H} values in references 57−59. (Bottom) plots of $(RT/F)\ln(k_2)$ against the oxidation potential (E_{OX}) of *p*-X-2,6-DTBP substrates; all for the reactions of **1b** (red) and **2b** (blue) with *p*-X-2,6-DTBP substrates (X = OCH_3, CH_3, $C(CH_3)_3$, H, Br, CN, NO_2). For **2b**, X = CN, NO_2 substrates were not included in trend lines (substrates in blue boxes).

3,3′,5,5′-tetra-*tert*-butyl-[1,1′-bis(cyclohexylidene)]-2,2′,5,5′-tetraene-4,4′-dione was detected in approximately 12% yield along with 2,6-di-*tert*-butyl-1,4-benzoquinone (Figures S30−S32). For *p*-X-2,6-DTBP, X = OCH_3, $C(CH_3)_3$, H, Br, CN, NO_2, the radical coupling product 3,3′,5,5′-tetra-*tert*-butyl-[1,1′-bis(cyclohexylidene)]-2,2′,5,5′-tetraene-4,4′-dione was detected along with 2,6-di-*tert*-butyl-1,4-benzoquinone (Figures S30−S32). For *p*-CH_3-2,6-DTBP, the oxidized product was identified as 2,6-di-*tert*-butyl-4-methylene-3,5-cyclohexadien-1-one (Figure S31). For 2,4,6-TTBP, the 2,4,6-tri-*tert*-butylphenoxyl radical was identified to form in approximately 100% yield according to electronic absorption spectroscopy (Figure S33). A KIE value of 3.2 was obtained from the reactions of **2b** with [*H*]-*p*-CH_3-2,6-DTBP and [*D*]-*p*-CH_3-2,6-DTBP substrates (Figure S35). The measured KIE is consistent with the O−H bond cleavage being rate-determining.

Using the same Hammett, Bell−Evans−Polanyi, and Marcus treatments employed for **1b**, we see a divergence between electron-rich and electron-poor phenol substrates for **2b** (Figure 6, Figure S36). For electron-rich substrates, there is a linear correlation when comparing the rate constants obtained with the respective σ^+, BDE_{O-H}, and $E_{1/2}$ values. Based on this and the respective slopes of the plots in Figure 6 (**1b**: −2.72, 0.78, −0.18; **2b**: −3.48, 0.89, −0.27), we surmise that there is an HAT or CPET mechanism for electron-rich substrates that were oxidized by **2b**. We also conclude that there is little to no difference in the reactivity properties of **1b** and **2b** toward this subset of phenol substrates.

In contrast, for *p*-X-2,6-DTBP (X = Br, CN, NO_2) the reactions were unexpectedly more rapid than for **1b**. We also obtained a poor trend line for the series *p*-X-2,6-DTBP (X = H, Br, CN, NO_2). We have therefore not fit these data points with a trendline. Previously reported $[Cu^{III}(OH)(L)]$ and $[Cu^{III}(O_2)(L)]^-$ complexes displayed similarly divergent kinetics of phenol oxidation, where electron-poor phenolic substrates displayed higher than expected rates of oxidation of phenols.[38,56] This was ascribed to a change in mechanism of phenol oxidation, where a HAT was postulated for electron-rich substrates, which demonstrated a linear correlation and negative slope in the Hammett plot. A nonconcerted PCET mechanism (separate proton and electron transfer) was postulated for electron-poor substrates, displaying a linear correlation and positive slope in the Hammett plot. The lack of a reliable correlation for the electron-poor substrates in Figure 6 leads us not to predict a mechanism of oxidation by **2b** for these substrates, but to tentatively attribute this observation to a change in mechanism that is possibly driven by rate-limiting proton transfer or a more complicated partial transfer of charge at rates faster than a H^+ transfer.

*Oxidative Activation of Hydrocarbon C−H Bonds by **1b** and **2b**.* Both **1b** and **2b** reacted readily with xanthene (200−400 equiv) in acetone at −40 °C (Figures S37−S38). Xanthone was identified as a product of these reactions (Figure S39), presumably formed from the reaction of the formed xanthyl radical and solvated dioxygen or adventitious water. The second-order rate constants (k_2) for the reaction of xanthene with **1b** and **2b** were 0.003 and 0.012 M^{-1} s^{-1}, respectively (Figure 7, Table 1). This demonstrated a small kinetic difference (4-fold) in the reactivity of the high-valent d^8 (Cu^{III}, **2b**) oxidant compared to that of the d^7 (Ni^{III}, **1b**) oxidant under the same conditions with the exact same supporting ligands. Further insight was not possible because the natural decay of **1b** at −40 °C was on the same rate order as its reaction with hydrocarbon substrates with greater BDE_{C-H} than xanthene. We were, therefore, unable to probe its reactivity toward hydrocarbons with stronger C−H bonds at −40 °C. **1b** was unstable at 25 °C, preventing exploration of its reactivity toward substrates with greater BDE_{C-H} at higher temperatures.

Compound **2b** was sufficiently stable at 25 °C to probe its reactivity with a series of hydrocarbons with varying BDE_{C-H} values (75.5−90 kcal/mol, Table S7, Figures S40 and S41).

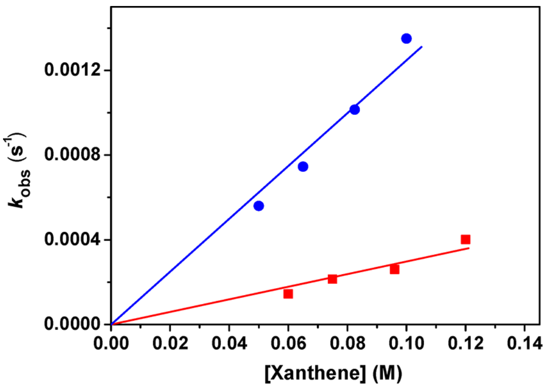

Figure 7. Plots of k_{obs} versus [xanthene] determined for the reactions between **1b** (red, k_2 = 0.003 M^{-1} s^{-1}) or **2b** (blue, k_2 = 0.012 M^{-1} s^{-1}) and xanthene at −40 °C in acetone.

For the oxidation of DHA, we have identified anthracene as the product. The yield of anthracene was 48% according to GC-FID (Figure S42). For CHD, benzene was identified as the product of oxidation, while for benzylalcohol, benzoic acid was identified in the post-reaction mixture (Figure S43). These products are typical of what is expected of a PCET oxidation of these substrates. C−H bond cleavage was predicted to be rate limiting because the measured KIE for the oxidation of 9,10-dihydroanthracene (DHA) and its deuterated analogue (Figure S45) was found to be KIE = 5.5. A plot of the log(k_2) versus substrate BDE_{C-H} was linear (Figure S44). Such correlation of the decrease in rate constants (k_2) with an increase in BDE_{C-H} is indicative of a HAT/CPET mechanism in the rate-limiting step. $\Delta G^{\ddagger}$ was calculated from the measured k_2 values and plotted against BDE_{C-H}. $BDFE_{O-H}$ values for all of these substrates in acetone were not available. For ease of comparison, we have plotted BDE_{O-H} (an enthalpy) against $\Delta G^{\ddagger}$ (a free energy, the differences in BDE/BDFE values are sufficiently small that the comparison is valid). A slope of 0.38 was measured (Figure 8), which was comparable to the value of 0.5 predicted by the Marcus theory for HAT.[19−21,60]

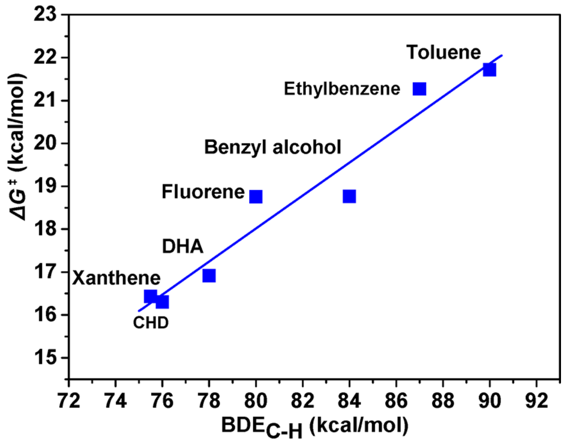

Figure 8. Plot of $\Delta G^{\ddagger}$ against the BDE_{C-H} for the reactions of **2b** with hydrocarbon substrates, measured at 25 °C (slope = 0.38). $BDFE_{O-H}$ values for all of these substrates in acetone were not available. For ease of comparison, we have plotted BDE_{O-H} (an enthalpy) against $\Delta G^{\ddagger}$ (a free energy). BDE_{C-H} values in references 61 and 62.

In order to compare Ni^{III} and Cu^{III} further, we have attempted to compare **2b** and the previously reported $[Ni^{III}(OAc)(L^*)]$ (Figure S49). We observed that **2b** consistently displayed k_2 values approximately 3- to 10-fold less than that of $[Ni^{III}(OAc)(L^*)]$. This contrasts with the observation that **2b** displayed a k_2 value 4-fold greater than that of **1b** in xanthene oxidation. To understand this and the influence of the ligand (L* in $[Ni^{III}(OAc)(L^*)]$, versus L in **1b** and **2b**), we measured the rate of xanthene oxidation by $[Ni^{III}(OAc)(L^*)]$ under the exact same conditions as for **1b** and **2b** (Table 1, Figure S50). The measured k_2 value (0.004 M^{-1} s^{-1}) was very close to that obtained for **1b** (0.003 M^{-1} s^{-1}). The comparison in Figure S49 is problematic because **2b** was prepared with magic blue in acetone at 25 °C, while $[Ni^{III}(OAc)(L^*)]$ was prepared with $NaOCl/H_2O/HO_2CCH_3$ in acetone at 25 °C. This precludes us from making a direct comparison of the relative rates of oxidation by **2b** and $[Ni^{III}(OAc)(L^*)]$ because we cannot gauge the effect of H_2O/HO_2CCH_3 on the rates of HAT oxidation. We assume the presence of these protons donors will cause differences in k_2 values. On the basis of the data currently on hand, we conclude that the metal ion has only a minor influence on the rate of HAT oxidation of hydrocarbons.

In order to understand the driving force for oxidation by **1b** and **2b** and any effect thereof on the k_2 values, we have attempted to calculate the $BDFE_{O-H}$ of the conjugate acids of **1a** and **2a** ($[Ni^{II}(HOAc)(L)]$ and $[Cu^{II}(HOAc)(L)]$), which are the presumed products formed by HAT/CPET oxidation by **1b** and **2b**, respectively (Scheme 1). At present, we do not have experimental evidence to show that ($[Ni^{II}(HOAc)(L)]$ and $[Cu^{II}(HOAc)(L)]$ are the products. The addition of Et_4NOAc to the post-reaction mixture results in an electronic absorption spectra typical of **1a** and **2a**, separately (Figure S46 and S47). This demonstrates that the [M(L)] unit remains intact during the oxidation reactions and supports our postulate that ($[Ni^{II}(HOAc)(L)]$ and $[Cu^{II}(HOAc)(L)]$ are the reduced products.

The calculation of $BDFE_{O-H}$ would be achieved through measuring the pK_a of the conjugate acids of **1a** and **2a**, and $E_{1/2}{}^{II/III}$ for **1a** and **2a**, and solving the following equation: $BDFE_{O-H} = 1.37\ (pK_a) + 23.06\ (E_{1/2}{}^{II/III}) + C_G$.[20,60] The $E_{1/2}{}^{II/III}$ has been measured for both **1a** and **2a** (Table 1, Figure S5), showing values of 0.32 and 0.17 V versus Fc^+/Fc, respectively. In an attempt to synthesize ($[Ni^{II}(HOAc)(L)]$ and $[Cu^{II}(HOAc)(L)]$, we reacted **1a** and **2a** with H^+ donors, and stable species were obtained. However, these were identified as the solvent adducts $[M^{II}(NCCH_3)(L)]$ (M = Ni, Cu) (Figure S48).[26,27] In alternative solvents (acetone and THF) we could not isolate a discrete complex. ^1H NMR indicated mixtures of at least 3 species. We therefore could not assess the pK_a of the conjugate acids of **1a** and **2a**. Unfortunately, this prevents us from measuring the $BDFE_{O-H}$ of the conjugate acids of **1a** and **2a** and thus assessing the role the $BDFE_{O-H}$ plays in comparing **1b** and **2b**.

For the reaction of **1b** and **2b** with 4-CH_3-2,6-DTBP, we have determined activation energy parameters (Figure S51). For **1b**, an activation enthalpy of $\Delta H^{\ddagger}$ = 4.5 kcal/mol was determined, while for **2b** $\Delta H^{\ddagger}$ = 7.6 kcal/mol. These values are reasonably close to one another indicating little to no difference in the activation enthalpy. In contrast, an activation entropy value for **1b** was determined to be $\Delta S^{\ddagger}$ = −43 cal mol^{-1} K^{-1}, and for **2b**, $\Delta S^{\ddagger}$ = −30 cal mol^{-1} K^{-1}. The magnitude of these values indicates that entropic factors play a significant role in the HAT/CPET reactions, as has been reported previously by Mayer and co-workers.[15,16] This was attributed to substantial contributions from vibrational energy, which varies between metals and is not commonly observed for organic radicals. This demonstrates that **1b** and **2b** behave similarly to previously reported oxidants but does not provide rationale for the lack of difference in their relative reactivity, which according to the above study should have been greater given the differences in redox potentials for their M$^{II/III}$ couples.

Discussion on Reactivity Properties. The goal of our reactivity studies was to compare the reactivity properties of high-valent Ni^{III} and Cu^{III} oxidants under the exact same conditions. Specifically, we were interested in how the metal ion and d-electron count can be utilized to modulate the reactivity in PCET oxidations.

The mechanism of oxidation of phenolic substrates by **1b** and **2b** followed a HAT or CPET mechanism, with both the Bell−Evans−Polanyi and Marcus treatments being in alignment with a HAT/CPET reaction (Figure 6). A direct comparison of the kinetic results for phenol oxidation by HAT/CPET by **1b** and **2b** indicated little to no difference. We observed that **2b** performed the oxidation of hydrocarbon substrates through a HAT/CPET mechanism. We could not assess the mechanism of hydrocarbon oxidation by **1b**, although we previously showed [Ni^{III}(OAc)(L*)] to perform hydrocarbon oxidation through HAT. We conclude that for both hydrocarbons and phenolic substrates there is little difference in the rate or mechanism of oxidation by these complexes.

A comparison of [Ni^{III}(OAc)(L*)] and [Ni^{III}(ONO$_2$)(L*)] yielded k_2 values in the oxidation of *p*-H-2,6-DTBP of 0.125 and 1.96 M^{-1} s^{-1}, respectively (a 20-fold difference).[23] These reactivity studies were performed under the exact same conditions as employed for **1b** and **2b** (0.24 and 0.09 M^{-1} s^{-1}, respectively). This represents a wide range of k_2 values upon simply exchanging the ancillary ligand and encourages us to make the postulate that the ancillary ligand will provide a greater degree of kinetic control, while exchanging the metal ion had almost no influence on the rate of reaction.

In the oxidation of DHA at 25 °C, the k_2 values for [Ni^{III}(OAc)(L*)] and **2b** were 8.11 and 2.46 M^{-1} s^{-1}, respectively. When compared to a large family of other high-valent oxidants, it places these M−O−X complexes at the more reactive end of the scale (Table 2). We note with interest the (estimated) superior rate at which [Cu^{III}(OH)(L)] reacted with DHA when compared to **2b**.[34] This would again suggest that the ancillary ligand has more influence in defining the kinetics of hydrocarbon oxidation.

Table 2. Comparison of k_2 for the Oxidation of DHA by High-Valent Oxidants[a]

	k_2 (M^{-1} s^{-1})	KIE	$\Delta G^{\ddagger}/\Delta G^{\circ}$ (BDFE)
2b	2.46	5.5	0.38
[Ni^{III}(OAc)(L*)]	8.11	3.0	0.31
[Cu^{III}(OH)(L)][34]	∼190	24	0.37
[Mn^{VII}O$_4$]$^{-}$[63,64]	0.12		0.69
[Mn^{IV}(Me$_2$EBC)(O)$_2$][65]	∼0.03	3.78	0.21
[Fe^{IV}(O)(N$_4$Py)]$^{2+}$[66]	18	20	0.15
[Fe^{III}(OCH$_3$)(PY5)]$^{2+}$[67]	0.0049	5.5	0.17
[Ru^{IV}(O)(bpy)$_2$(py)]$^{2+}$[61]	125	50−100	0.47

[a] For [Mn^{IV}(Me$_2$EBC)(O)$_2$] and [Cu^{III}(OH)(L)], data at 25 °C was not available: Values were derived from the experimentally determined activation parameters via the Eyring equation.

From the perspective of how strong a bond the oxidants are capable of activating, under the conditions applied herein, there was no difference in the capabilities of **1b**, **2b**, and [Ni^{III}(OX)(L*)]. Both **2b** and [Ni^{III}(OX)(L*)] were capable of activating the C−H bond of toluene, but no other substrates containing higher BDE$_{C-H}$. Likewise, all three complexes were capable of activating the O−H bond in *p*-NO$_2$-2,6-DTBP, with the highest BDE$_{O-H}$ in the *p*-X-2,6-DTBP series.

We have observed little difference in the rate constants for **1b** and **2b**. We previously identified that exchanging the ONO$_2$ for OAc on Ni^{III} resulted in rate enhancements that could be attributed to a lower kinetic barrier or greater thermodynamic driving force. We postulate that the product of the HAT oxidation by these complexes is their M^{II}-conjugate acid complex, and the magnitude of the BDFE$_{O-H}$ in this complex could drive the oxidation reaction. Unfortunately, we cannot assess the difference in the magnitude of the BDFE$_{O-H}$ of the conjugate acids for **1a**, **2a**, [NiII(OAc)(L*)]$^{-}$, and [NiII(ONO$_2$)(L*)]$^{-}$. The BDE$_{O-H}$ values for HOAc, HNO$_3$, and H$_2$O have been measured (112, 102, 119 kcal/mol, respectively),[68] and if we exclude from consideration the influence of the metal ion, allow us to suggest that M−OH complexes should demonstrate the highest thermodynamic driving force for HAT and ONO$_2$ the lowest. This is supported by the observation that [Cu^{III}(OH)(L)][34] displayed some of the highest rates of substrate oxidation but contradicted by [Ni^{III}(ONO$_2$)(L*)] ≫ [Ni^{III}(OAc)(L*)]. This leads us to surmise that the ancillary ligand, in some cases, may lower the kinetic barrier to the PCET activation of C−H and O−H bonds, while in this case the metal has little influence on the kinetics of substrate oxidation.

■ CONCLUSIONS

We have synthesized and characterized two high-valent species: a d^7 Ni^{III} complex (**1b**) and a d^8 Cu^{III} complex (**2b**). Both complexes were characterized through electronic absorption, EPR, and XAS spectroscopies, mass spectrometry, and DFT calculations. The reactivity of **1b** and **2b** toward a series of *para*-substituted phenols (*p*-X-2,6-DTBP; X = OCH$_3$, C(CH$_3$)$_3$, CH$_3$, H, Br, CN, NO$_2$) was studied, showing similar rates of reaction for both complexes and a HAT/CPET mechanism of substrate oxidation. In hydrocarbon oxidation, the d^8 Cu^{III} oxidant displayed a small (4-fold) increase in the rate constant compared to that of the d^7 Ni^{III} oxidant in the oxidation of xanthene. The d^8 Cu^{III} oxidant was capable of oxidizing a large family of hydrocarbon substrates through a HAT/CPET mechanism. Overall, it was concluded that the metal ion had a small impact on the rate of HAT/CPET oxidation, while, in this instance, the nature of ancillary donor ligand appears to yield considerably more kinetic control over HAT/CPET oxidation. Our findings provide insight into high-valent transition metal oxidants in biology and synthetic oxidation catalysis.

■ ASSOCIATED CONTENT

Ⓢ Supporting Information

The Supporting Information is available free of charge at https://pubs.acs.org/doi/10.1021/acs.inorgchem.9b03101.

Physical methods, cyclic voltammetry, EPR spectroscopy, X-ray crystallography, ESI-MS analysis, XAS methods, quantum chemical calculations, materials, preparation methods, reactivity protocols, schemes of products, general procedures, figures of NMR spectra, ATR-FTIR spectra, ESI-MS spectra, cyclic voltammograms, electronic absorption spectra, X-band EPR spectra, second derivative spectra, EXAFS data, plots, UV−vis absorption spectra, APCI mass spectra, monitored reactions, Hammett correlation plots, ESI-TOF mass spectra, optimized molecular structure, and spin density plots, tables of crystal data and structure refinement parameters, selected bond distances and angles, selected EXAFS data, substrate properties and rate constants, dissociation energies, and atomic coordinates (PDF)

Accession Codes

CCDC 1915020−1915021 contain the supplementary crystallographic data for this paper. These data can be obtained free of charge via www.ccdc.cam.ac.uk/data_request/cif, or by emailing data_request@ccdc.cam.ac.uk, or by contacting The Cambridge Crystallographic Data Centre, 12 Union Road, Cambridge CB2 1EZ, UK; fax: +44 1223 336033.

AUTHOR INFORMATION

Corresponding Author

*E-mail: aidan.mcdonald@tcd.ie.

ORCID

Aidan R. McDonald: 0000-0002-8930-3256

Author Contributions

§R.G., M.L., and D.N. contributed equally.

Notes

The authors declare no competing financial interest.

ACKNOWLEDGMENTS

This publication has emanated from research supported by the European Research Council (ERC-2015-STG-678202). Research in the McDonald lab is supported in part by a research grant from Science Foundation Ireland (SFI/15/RS-URF/3307). XAS experiments were conducted at SSRL beamline 7-3 (SLAC National Accelerator Laboratory, USA), with support from the DOE Office of Science (DE-AC02-76SF00515), DOE Office of Biological and Environmental Research, and NIH (P41-GM-103393 and P30-EB-009998). We are grateful to COST Action CM1305 (ECOSTBio) for networking support. We thank Prof. Robert Barkley for training on and use of an EPR spectrometer. We wish to acknowledge the Irish Centre for High-End Computing (ICHEC) for the provision of computational facilities and support.

REFERENCES

(1) Bordeaux, M.; Galarneau, A.; Drone, J. Catalytic, Mild, and Selective Oxyfunctionalization of Linear Alkanes: Current Challenges. *Angew. Chem., Int. Ed.* **2012**, *51* (43), 10712−10723.

(2) Goldberg, K. I.; Goldman, A. S. Large-Scale Selective Functionalization of Alkanes. *Acc. Chem. Res.* **2017**, *50* (3), 620−626.

(3) Costas, M.; Mehn, M. P.; Jensen, M. P.; Que, L. Dioxygen activation at mononuclear nonheme iron active sites: enzymes, models, and intermediates. *Chem. Rev.* **2004**, *104*, 939−986.

(4) Hausinger, R. P. FeII/alpha-ketoglutarate-dependent hydroxylases and related enzymes. *Crit. Rev. Biochem. Mol. Biol.* **2004**, *39*, 21−68.

(5) Solomon, E. I.; Szilagyi, R. K.; DeBeer George, S.; Basumallick, L. Electronic Structures of Metal Sites in Proteins and Models: Contributions to Function in Blue Copper Proteins. *Chem. Rev.* **2004**, *104* (2), 419−458.

(6) Can, M.; Armstrong, F. A.; Ragsdale, S. W. Structure, Function, and Mechanism of the Nickel Metalloenzymes, CO Dehydrogenase, and Acetyl-CoA Synthase. *Chem. Rev.* **2014**, *114*, 4149.

(7) Poulos, T. L. Heme Enzyme Structure and Function. *Chem. Rev.* **2014**, *114*, 3919.

(8) Solomon, E. I.; Heppner, D. E.; Johnston, E. M.; Ginsbach, J. W.; Cirera, J.; Qayyum, M.; Kieber-Emmons, M. T.; Kjaergaard, C. H.; Hadt, R. G.; Tian, L. Copper Active Sites in Biology. *Chem. Rev.* **2014**, *114*, 3659.

(9) Lewis, E. A.; Tolman, W. B. Reactivity of Dioxygen-Copper Systems. *Chem. Rev.* **2004**, *104* (2), 1047−1076.

(10) Mirica, L. M.; Ottenwaelder, X.; Stack, T. D. P. Structure and Spectroscopy of Copper-Dioxygen Complexes. *Chem. Rev.* **2004**, *104* (2), 1013−1046.

(11) Tshuva, E. Y.; Lippard, S. J. Synthetic Models for Non-Heme Carboxylate-Bridged Diiron Metalloproteins: Strategies and Tactics. *Chem. Rev.* **2004**, *104* (2), 987−1012.

(12) Wu, A. J.; Penner-Hahn, J. E.; Pecoraro, V. L. Structural, Spectroscopic, and Reactivity Models for the Manganese Catalases. *Chem. Rev.* **2004**, *104* (2), 903−938.

(13) McDonald, A. R.; Que Jr, L. High-valent nonheme iron-oxo complexes: Synthesis, structure, and spectroscopy. *Coord. Chem. Rev.* **2013**, *257* (2), 414−428.

(14) Elwell, C. E.; Gagnon, N. L.; Neisen, B. D.; Dhar, D.; Spaeth, A. D.; Yee, G. M.; Tolman, W. B. Copper-Oxygen Complexes Revisited: Structures, Spectroscopy, and Reactivity. *Chem. Rev.* **2017**, *117* (3), 2059−2107.

(15) Mader, E. A.; Manner, V. W.; Markle, T. F.; Wu, A.; Franz, J. A.; Mayer, J. M. Trends in Ground-State Entropies for Transition Metal Based Hydrogen Atom Transfer Reactions. *J. Am. Chem. Soc.* **2009**, *131* (4), 4335−4345.

(16) Mader, E. A.; Davidson, E. R.; Mayer, J. M. Large Ground-State Entropy Changes for Hydrogen Atom Transfer Reactions of Iron Complexes. *J. Am. Chem. Soc.* **2007**, *129* (16), 5153−5166.

(17) Smeets, P. J.; Woertink, J. S.; Sels, B. F.; Solomon, E. I.; Schoonheydt, R. A. Transition-Metal Ions in Zeolites: Coordination and Activation of Oxygen. *Inorg. Chem.* **2010**, *49* (8), 3573−3583.

(18) Snyder, B. E. R.; Bols, M. L.; Schoonheydt, R. A.; Sels, B. F.; Solomon, E. I. Iron and Copper Active Sites in Zeolites and Their Correlation to Metalloenzymes. *Chem. Rev.* **2018**, *118* (5), 2718−2768.

(19) Mayer, J. M. Understanding Hydrogen Atom Transfer: From Bond Strengths to Marcus Theory. *Acc. Chem. Res.* **2011**, *44* (1), 36−46.

(20) Warren, J. J.; Tronic, T. A.; Mayer, J. M. Thermochemistry of Proton-Coupled Electron Transfer Reagents and its Implications. *Chem. Rev.* **2010**, *110* (12), 6961−7001.

(21) Darcy, J. W.; Koronkiewicz, B.; Parada, G. A.; Mayer, J. M. A Continuum of Proton-Coupled Electron Transfer Reactivity. *Acc. Chem. Res.* **2018**, *51* (10), 2391−2399.

(22) Pirovano, P.; Farquhar, E. R.; Swart, M.; Fitzpatrick, A. J.; Morgan, G. G.; McDonald, A. R. Characterization and Reactivity of a Terminal Nickel(III)-Oxygen Adduct. *Chem. - Eur. J.* **2015**, *21*, 3785−3790.

(23) Pirovano, P.; Farquhar, E. R.; Swart, M.; McDonald, A. R. Tuning the Reactivity of Terminal Nickel(III)-Oxygen Adducts for C-H Bond Activation. *J. Am. Chem. Soc.* **2016**, *138* (43), 14362−14370.

(24) Mondal, P.; Pirovano, P.; Das, A.; Farquhar, E. R.; McDonald, A. R. Hydrogen Atom Transfer by a High-Valent Nickel-Chloride Complex. *J. Am. Chem. Soc.* **2018**, *140* (5), 1834−1841.

(25) Pirovano, P.; Twamley, B.; McDonald, A. R. Modulation of Nickel Pyridinedicarboxamidate Complexes to Explore the Properties of High-valent Oxidants. *Chem. - Eur. J.* **2018**, *24* (20), 5238−5245.

(26) Pirovano, P.; Berry, A. R.; Swart, M.; McDonald, A. R. Indirect evidence for a Ni(III)-oxyl oxidant in the reaction of a Ni(II) complex with peracid. *Dalton Trans.* **2018**, *47* (1), 246−250.

(27) Donoghue, P. J.; Gupta, A. K.; Boyce, D. W.; Cramer, C. J.; Tolman, W. B. An anionic, tetragonal copper(II) superoxide complex. *J. Am. Chem. Soc.* **2010**, *132*, 15869−15871.

(28) Yang, L.; Powell, D. R.; Houser, R. P. *Dalton Trans.* **2007**, 955.

(29) Huang, D.; Holm, R. H. Reactions of the terminal Ni(II)-OH group in substitution and electrophilic reactions with carbon dioxide and other substrates: structural definition of binding modes in an intramolecular Ni(II)···Fe(II) bridged site. *J. Am. Chem. Soc.* **2010**, *132*, 4693−4701.

(30) Corona, T.; Pfaff, F. F.; Acuña-Parés, F.; Draksharapu, A.; Whiteoak, C. J.; Martin-Diaconescu, V.; Lloret-Fillol, J.; Browne, W. R.; Ray, K.; Company, A. Reactivity of a Nickel(II) Bis(amidate) Complex with *meta*-Chloroperbenzoic Acid: Formation of a Potent Oxidizing Species. *Chem. - Eur. J.* **2015**, *21* (42), 15029−15038.

(31) Corona, T.; Company, A. Spectroscopically Characterized Synthetic Mononuclear Nickel-Oxygen Species. *Chem. - Eur. J.* **2016**, *22* (38), 13422−13429.

(32) Corona, T.; Draksharapu, A.; Padamati, S. K.; Gamba, I.; Martin-Diaconescu, V.; Acuña-Parés, F.; Browne, W. R.; Company, A. Rapid Hydrogen and Oxygen Atom Transfer by a High-Valent Nickel-Oxygen Species. *J. Am. Chem. Soc.* **2016**, *138* (39), 12987−12996.

(33) Pirovano, P.; McDonald, A. R. Synthetic High-Valent M-O-X Oxidants. *Eur. J. Inorg. Chem.* **2018**, *2018* (5), 547−560.

(34) Donoghue, P. J.; Tehranchi, J.; Cramer, C. J.; Sarangi, R.; Solomon, E. I.; Tolman, W. B. Rapid C-H bond activation by a monocopper(III)-hydroxide complex. *J. Am. Chem. Soc.* **2011**, *133*, 17602−17605.

(35) Dhar, D.; Tolman, W. B. Hydrogen Atom Abstraction from Hydrocarbons by a Copper(III)-Hydroxide Complex. *J. Am. Chem. Soc.* **2015**, *137* (3), 1322−1329.

(36) Gagnon, N.; Tolman, W. B. $[CuO]^+$ and $[CuOH]^{2+}$ complexes: intermediates in oxidation catalysis? *Acc. Chem. Res.* **2015**, *48* (7), 2126−2131.

(37) Dhar, D.; Yee, G. M.; Spaeth, A. D.; Boyce, D. W.; Zhang, H.; Dereli, B.; Cramer, C. J.; Tolman, W. B. Perturbing the Copper(III)-Hydroxide Unit through Ligand Structural Variation. *J. Am. Chem. Soc.* **2016**, *138* (1), 356−368.

(38) Dhar, D.; Yee, G. M.; Markle, T. F.; Mayer, J. M.; Tolman, W. B. Reactivity of the copper(III)-hydroxide unit with phenols. *Chem. Sci.* **2017**, *8* (2), 1075−1085.

(39) Kau, L. s.; Spira-Solomon, D. J.; Spira-Solomon-Penner-Hahn, J. E.; Hodgson, K. O.; Solomon, E. I. X-ray Absorption Edge Determination of the Oxidation State and Coordination Number of Copper: Application to the Type 3 Site in Rhus vernicifera Laccase and Its Reaction with Oxygen. *J. Am. Chem. Soc.* **1987**, *109* (21), 6433−6442.

(40) Chang, H. C.; Lo, F. C.; Liu, W. C.; Lin, T. H.; Liaw, W. F.; Kuo, T. S.; Lee, W. Z. Ambient stable trigonal bipyramidal copper(III) complexes equipped with an exchangeable axial ligand. *Inorg. Chem.* **2015**, *54* (11), 5527−5533.

(41) DuBois, J. L.; Mukherjee, P.; Colier, A. M.; Mayer, J. M.; Solomon, E. I.; Hedman, B.; Stack, T. D. P.; Hodgson, K. O. Cu K-edge XAS study of the $[Cu_2(\mu\text{-}O)_2]$ core: Direct experimental evidence for the presence of Cu(III). *J. Am. Chem. Soc.* **1997**, *119* (36), 8578−8579.

(42) Sarangi, R.; Aboelella, N.; Fujisawa, K.; Tolman, W. B.; Hedman, B.; Hodgson, K. O.; Solomon, E. I. X-ray Absorption Edge Spectroscopy and Computational Studies on $LCuO_2$ Species: Superoxide-Cu^{II} versus Peroxide-Cu^{III} Bonding. *J. Am. Chem. Soc.* **2006**, *128*, 8286−8296.

(43) Sarangi, R.; George, S. D. B.; Rudd, D. J.; Szilagyi, R. K.; Ribas, X.; Rovira, C.; Almeida, M.; Hodgson, K. O.; Hedman, B.; Solomon, E. I. Sulfur K-edge X-ray absorption spectroscopy as a probe of ligand-metal bond covalency: Metal vs ligand oxidation in copper and nickel dithiolene complexes. *J. Am. Chem. Soc.* **2007**, *129* (8), 2316−2326.

(44) Aboelella, N. W.; Kryatov, S. V.; Gherman, B. F.; Brennessel, W. W.; Young, V. G., Jr.; Sarangi, R.; Rybak-Akimova, E. V.; Hodgson, K. O.; Hedman, B.; Solomon, E. I.; Cramer, C. J.; Tolman, W. B. Dioxygen Activation at a Single Copper Site: Structure, Bonding, and Mechanism of Formation of 1:1 Cu-O_2 Adducts. *J. Am. Chem. Soc.* **2004**, *126*, 16896−16911.

(45) As the copper foil reference for these measurements was calibrated to 8979 eV, as opposed to the conventional 8980.3 eV, this causes all of the values to be red-shifted by 1.3 eV. Hence, if the reference foil had been set at 8980.3 eV, as is convention, the values obtained for the pre-edge would be 8979.4 eV for **1a** and 8980.7 eV for **1b**. This is within the average range of 8979 (±0.4 eV) for Cu^{II} and 8981 (±0.5 eV) for Cu^{III}.

(46) DuBois, J. L.; Mukherjee, P.; Stack, T. D. P.; Hedman, B.; Solomon, E. I.; Hodgson, K. O. A Systematic K-edge X-ray Absorption Spectroscopic Study of Cu(III) Sites. *J. Am. Chem. Soc.* **2000**, *122*, 5775−5787.

(47) Lytle, F. W.; Greegor, R. B.; Panson, J. Discussion of x-ray absorption near edge structure: Application to Cu in the high-Tc superconductors $La_{1.8}Sr_{0.2}CuO_4$ and $YBa_2Cu_3O_7$. *Phys. Rev. B: Condens. Matter Mater. Phys.* **1988**, *37* (4), 1550−1563.

(48) McManus, C.; Mondal, P.; Lovisari, M.; Twamley, B.; McDonald, A. R. Carboxamidate Ligand Noninnocence in Proton Coupled Electron Transfer. *Inorg. Chem.* **2019**, *58* (7), 4515−4523.

(49) Guttenplan, J. B.; Cohen, S. G. Triplet energies, reduction potentials, and ionization potentials in carbonyl-donor partial charge-transfer interactions. *J. Am. Chem. Soc.* **1972**, *94* (11), 4040−4042.

(50) Wagner, P. J.; Lam, H. M. H. Charge-transfer quenching of triplet 5-trifluoroacetophenones. *J. Am. Chem. Soc.* **1980**, *102* (12), 4167−4172.

(51) Marcus, R. A.; Sutin, N. Electron transfers in chemistry and biology. *Biochim. Biophys. Acta, Rev. Bioenerg.* **1985**, *811* (3), 265−322.

(52) Ram, M. S.; Hupp, J. T. Linear free energy relations for multielectron transfer kinetics: a brief look at the Broensted/Tafel analogy. *J. Phys. Chem.* **1990**, *94* (6), 2378−2380.

(53) Weatherly, S. C.; Yang, I. V.; Thorp, H. H. Proton-Coupled Electron Transfer in Duplex DNA: Driving Force Dependence and Isotope Effects on Electrocatalytic Oxidation of Guanine. *J. Am. Chem. Soc.* **2001**, *123* (6), 1236−1237.

(54) Lee, J. Y.; Peterson, R. L.; Ohkubo, K.; Garcia-Bosch, I.; Himes, R. a.; Woertink, J.; Moore, C. D.; Solomon, E. I.; Fukuzumi, S.; Karlin, K. D. Mechanistic insights into the oxidation of substituted phenols via hydrogen atom abstraction by a cupric-superoxo complex. *J. Am. Chem. Soc.* **2014**, *136*, 9925−9937.

(55) Garcia-Bosch, I.; Cowley, R. E.; Díaz, D. E.; Peterson, R. L.; Solomon, E. I.; Karlin, K. D. Substrate and Lewis Acid Coordination Promote O-O Bond Cleavage of an Unreactive $L_2Cu^{II}{}_2(O_2{}^{2-})$ Species to Form $L_2Cu^{III}{}_2(O)_2$ Cores with Enhanced Oxidative Reactivity. *J. Am. Chem. Soc.* **2017**, *139* (8), 3186−3195.

(56) Bailey, W. D.; Dhar, D.; Cramblitt, A. C.; Tolman, W. B. Mechanistic Dichotomy in Proton-Coupled Electron-Transfer Reactions of Phenols with a Copper Superoxide Complex. *J. Am. Chem. Soc.* **2019**, *141* (13), 5470−5480.

(57) Luo, Y.-R. *Handbook of Bond Dissociation Energies in Organic Compounds*; CRC Press, 2002.

(58) Brigati, G.; Lucarini, M.; Mugnaini, V.; Pedulli, G. F. Determination of the Substituent Effect on the O-H Bond Dissociation Enthalpies of Phenolic Antioxidants by the EPR Radical Equilibration Technique. *J. Org. Chem.* **2002**, *67* (14), 4828−4832.

(59) Kundu, S.; Miceli, E.; Farquhar, E. R.; Ray, K. Mechanism of phenol oxidation by heterodinuclear NiCu bis(μ-oxo) complexes involving nucleophilic oxo groups. *Dalton Trans.* **2014**, *43*, 4264−4267.

(60) Mayer, J. M. Understanding hydrogen atom transfer: from bond strengths to Marcus theory. *Acc. Chem. Res.* **2011**, *44*, 36−46.

(61) Bryant, J. R.; Mayer, J. M. Oxidation of C-H Bonds by $[(bpy)_2(py)Ru^{IV}O]^{2+}$ Occurs by Hydrogen Atom Abstraction. *J. Am. Chem. Soc.* **2003**, *125* (34), 10351−10361.

(62) Brandi, P.; Galli, C.; Gentili, P. Kinetic Study of the Hydrogen Abstraction Reaction of the Benzotriazole-N-oxyl Radical (BTNO) with H-Donor Substrates. *J. Org. Chem.* **2005**, *70* (23), 9521−9528.

(63) Mandal, D.; Ramanan, R.; Usharani, D.; Janardanan, D.; Wang, B.; Shaik, S. How Does Tunneling Contribute to Counterintuitive H-Abstraction Reactivity of Nonheme Fe(IV)O Oxidants with Alkanes? *J. Am. Chem. Soc.* **2015**, *137* (2), 722−733.

(64) Mandal, D.; Shaik, S. Interplay of Tunneling, Two-State Reactivity, and Bell-Evans-Polanyi Effects in C-H Activation by Nonheme Fe(IV)O Oxidants. *J. Am. Chem. Soc.* **2016**, *138* (7), 2094−2097.

(65) Yin, G.; Danby, A. M.; Kitko, D.; Carter, J. D.; Scheper, W. M.; Busch, D. H. Oxidative Reactivity Difference among the Metal Oxo and Metal Hydroxo Moieties: pH Dependent Hydrogen Abstraction by a Manganese(IV) Complex Having Two Hydroxide Ligands. *J. Am. Chem. Soc.* **2008**, *130*, 16245−16253.

(66) Klinker, E. J.; Shaik, S.; Hirao, H.; Que, L. A Two-State Reactivity Model Explains Unusual Kinetic Isotope Effect Patterns in C-H Bond Cleavage by Nonheme Oxoiron(IV) Complexes. *Angew. Chem., Int. Ed.* **2009**, *48* (7), 1291−1295.

(67) Goldsmith, C. R.; Jonas, R. T.; Stack, T. D. P. C-H Bond Activation by a Ferric Methoxide Complex: Modeling the Rate-Determining Step in the Mechanism of Lipoxygenase. *J. Am. Chem. Soc.* **2002**, *124* (1), 83−96.

(68) Blanksby, S. J.; Ellison, G. B. Bond Dissociation Energies of Organic Molecules. *Acc. Chem. Res.* **2003**, *36*, 255−263.